

Thermal super-jogs control high-temperature strength in Nb-Mo-Ta-W alloys

Sicong He^a, Xinran Zhou^a, Dan Mordehai^b, Jaime Marian^{a,c}

^aDepartment of Materials Science and Engineering, University of California, Los Angeles, CA 90095, USA

^bDepartment of Mechanical Engineering, Technion-Israel Institute of Technology, Haifa 3200003, Israel

^cDepartment of Mechanical and Aerospace Engineering, University of California, Los Angeles, CA 90095, USA

Abstract

Refractory multi-element alloys (RMEA) with body-centered cubic (bcc) structure have been the object of much research over the last decade due to their high potential as candidate materials for high-temperature applications. Most of these alloys display a remarkable strength at temperatures above 1000°C, which cannot be explained by the standard model of bcc plasticity dominated by thermally-activated screw dislocation motion. Recent research on Nb-Mo-Ta-W alloys points to a heightened role of edge dislocations during mechanical deformation, which is generally attributed to atomic-level chemical fluctuations in the material and their interactions with dislocation cores during slip. However, while this effect accounts for levels of strength that are much larger than what might be found in a pure metal, it is not sufficient to explain the high yield stress found at high temperature in Nb-Mo-Ta-W. In this work, we propose a new strengthening mechanism based on the existence of thermal super-jogs in edge dislocation lines that act as strong obstacles to dislocation motion, conferring an extra strength to the alloy that turns out to be in very good agreement with experimental measurements. The basis for the formation of these super-jogs is found in the unique properties of RMEA, which display vacancy formation energy distributions with tails that extend into negative values. This leads to spontaneous, i.e., athermal, vacancy formation at edge dislocation cores, which subsequently relax into atomic-sized super-jogs on the dislocation line. At the same time, these super-jogs can displace diffusively along the glide direction, relieving with their motion some of the extra stress, thus countering the hardening effect due to jog-pinning. We implement these mechanisms into a specially-designed hybrid kinetic Monte Carlo/Discrete Dislocation Dynamics approach (kMC/DD) parameterized with vacancy formation and migration energy distributions obtained with machine-learning potentials designed specifically for the Nb-Mo-Ta-W system. The kMC module sets the timescale dictated by thermally-activated events, while the DD module relaxes the dislocation line configuration in between events in accordance with the applied stress. We find that the balance between super-jog pinning and super-jog diffusion confers an extra strength to edge dislocations at intermediate-to-high temperatures that is in remarkable agreement with experimental measurements in equiatomic Nb-Mo-Ta-W and several other RMEA. We derive an analytical model based on the computational results that captures this improved understanding of plastic processes in these alloys and explains the experimental data.

Keywords: Multielement alloys; High entropy alloys; Edge dislocations; Kinetic Monte Carlo simulations; Strength of materials; Dislocation dynamics

1. Introduction

Since their inception in the 1990s [1, 2], high entropy alloys (HEA) have attracted a great deal of attention due to a unique combination of properties seldom found in other material types [3–11]. This makes them potentially very attractive as candidate materials for a number of technological applications in harsh environments such as elevated temperatures, irradiation, or corrosion [12–15]. The basic idea behind creating alloys of this type is to combine a number of elements (typically four or more) in similar proportions to achieve solid solution phase stability through the large configurational entropy of the system. Due to the large chemical and configurational space available to create

Email address: jmarian@ucla.edu (Jaime Marian)

these materials, several hundred different HEA combinations now exist, each with their own distinct compositions, structure, and properties [16–18]. The large volume of research on the topic over the last decade has resulted in a fast-evolving field full of new findings, unexplained results, and unresolved controversies. The reader is referred to the numerous reviews and monographs published over the last several years for more details [3–10, 19, 20]. Note that, while the term ‘multicomponent’ or ‘multielement’ alloys is sometimes preferred in the literature over ‘high-entropy’ alloys (particularly when the number of elemental constituents is less than five), here we use all interchangeably.

Among the different materials proposed, refractory multi-element alloys (RMEA) are a special class of alloys composed of typically four or more refractory metal elements (Nb, Mo, Ta, V, W, Cr, Hf, Zr). These systems generally crystallize into a single body-centered cubic (bcc) phase, found to be stable up to very high temperatures [9, 21–27]. RMEA display sluggish self-diffusion rates [28–31] and, similar to their pure bcc metal counterparts, suffer from a lack of ductility at low temperatures [21, 32]. However, they retain a high strength and ductility at high temperature, making them attractive candidates for structural applications in the power, aerospace, or nuclear sector [12–14, 19, 33].

While the deformation mechanisms of bcc metals and their alloys are relatively well understood, the mechanical response of chemically complex alloys at high temperature is still under vigorous investigation. Perhaps one of the most crucial aspects separating standard bcc behavior with that of RMEA is the role played by screw and edge dislocations during plastic deformation. Although the experimental evidence is still inconclusive [34–36], recent research points to the increased importance of edge dislocation slip relative their role in pure metal bcc systems and dilute alloys [37–40]. Because chemical fluctuations in HEA take place at the atomistic scale, molecular dynamics (MD) has become the preferred tool to simulate dislocation processes in these systems. Indeed, MD simulations have been used to characterize the intrinsic roughness of dislocation lines [37, 41, 42], the effect of short-range order (SRO) [37, 40, 43] on alloy properties, and dislocation mobilities [40, 44]. For example, MD simulations have convincingly shown that the lattice resistance aided by SRO (intrinsic strengthening) in bcc RMEA can reach up to 1 GPa at low temperatures. However, their contribution is much diminished as the temperature increases, and it alone cannot account for the observed high-temperature dependence of alloy strength.

In contrast, an often overlooked feature of multi-element systems is the statistical nature of defect properties due to their compositional heterogeneity [45–49]. Properties such as point defect formation energies, planar defect energies, or dislocation core energies are defined by distributions whose variance generally correlates with the number of elements in the alloy [47, 48]. In particular, the thermal concentration of point defects in pure refractory metals is typically negligible on account of their relatively high formation energies. However, in HEA the low energy tails of defect energy distributions can lead to non-insignificant defect concentrations, even in conditions where these would be several orders of magnitude lower if one considered only the individual alloy elements. Moreover, defect formation energies can be substantially reduced at material inhomogeneities such as dislocation cores, material interfaces, precipitates, etc. [50, 51]. For vacancies, which display formation energies 2~3 times lower than self-interstitial atoms in metals, a side effect of above two effects combined (broad energy distributions together with heterogeneous defect nucleation), is the possibility for non-thermal formation, i.e., the spontaneous existence of vacancies at any temperature at pre-existing microstructural defects.

Of particular interest is the formation of vacancies at or near edge dislocation cores, which is thermodynamically more favorable within the compressive region of the stress field [51]. Topologically, vacancies on dislocation lines can be regarded as elementary (super)jogs that can only move by nonconservative means (e.g., *jog dragging*) [52–54]. As such, the existence of super-jogs on a dislocation line can lead to extra strengthening, as has been seen in a number of systems at high temperature [55]. Moreover, owing to the low energy tails of the vacancy formation energy distributions, it is reasonable to expect a nonzero concentration of super-jogs on edge dislocation lines in even at low temperatures. The main objective of this work is to quantify this specific effect in a model RMEA and establish its viability as a high-temperature strengthening mechanism. More generally, we aim to study the behavior of edge dislocations, and their impact on alloy strength, when single-valued point defect energies are replaced by energy distributions.

Due to MD’s intrinsic limitations when it comes to simulating thermally-activated mechanisms and their role in dislocation motion, here, following our line of work in previous publications [56, 57], we conduct stress-driven simulations of edge dislocation motion as a function of temperature using a combined approach consisting of discrete dislocation dynamics (DD) and kinetic Monte Carlo (kMC). Our DD/kMC model captures the thermal formation and evolution of vacancies/super-jogs on edge dislocations and quantifies their effect on dislocation motion as a first attempt to embed some of the complexities of the highly-random alloy into a mesoscale framework with the aim of

capturing time and length scales more suitable for experiments, as compared to MD. We focus on equiatomic Nb-Mo-Ta-W alloys, for which robust interatomic potentials exist [58–60], as well as a wealth of experimental data [24, 61–65], and carry out calculations of vacancy energetics to parameterize the model without fitting to any experimental measurements.

The paper is organized as follows. First, we provide the theoretical framework for DD/kMC model. This is followed by a description of the numerical implementation and the atomistic calculations performed to parameterize the model to the alloy of choice. Next we present results of the strength of the alloy as a function of temperature and strain rate. We finalize the paper with a discussion of the results and the conclusions.

2. Theory and models

2.1. Monte Carlo model of non-conservative edge dislocation motion

The key element of the modeling approach is a stochastic model based on the residence-time algorithm to simulate dislocation evolution under stress. The time scale is governed by a set of thermally-activated events that punctuate periods of standard dislocation glide. As such, dislocation evolution proceeds by way of a series of super-jog processes intercalated by stress-assisted glide. Here we consider two distinct thermal processes, which are schematically illustrated in Figure 1:

1. At any point during a simulation, a super-jog may appear on the dislocation line by thermal nucleation of a vacancy (process shown in Fig. 1a). Such nucleation is subjected to equilibrium constraints so that the linear concentration of super-jogs remains within thermal limits. For this, the dislocation line is subdivided into irreducible segments of length $w = \frac{a_0\sqrt{6}}{3}$ (equal to the periodicity along the line direction $1/6\langle 112 \rangle$), where a_0 is the lattice parameter. The insertion rate of super-jogs per unit length is:

$$q_n^{\text{jog}}(T; t) = \nu_0 \left[\frac{\ell}{w} - n(t) \right] \left(1 - \frac{n(t)}{n_0(T)} \right) \quad (1)$$

where T is the absolute temperature, ν_0 is a temperature-independent vacancy nucleation attempt frequency, $n(t)$ is the number of super-jogs at time t (the current number of super-jogs), and $n_0(T)$ is the equilibrium super-jog concentration (to be defined in Section 2.3). Here, the ratio ℓ/w represents the number of potential nucleation sites on a dislocation with total length ℓ for a super-jog to form, while $[\ell/w - n(t)] > 0$ represents the number of available nucleation sites¹. The ‘height’ of a jog segment is the unit lattice parameter along the y -direction: $h = \|1/2[110]\| = a_0\sqrt{2}/2$. Note that, while thermodynamically possible, super-jog reabsorption is highly unlikely because it requires either the arrival of self-interstitial atoms or emission of vacancies, both of which are discarded in this model due to their high penalizing energies.

2. Existing super-jogs can translate along the glide x -direction via diffusive jumps to a location separated one Burgers vector’s distance from the original position (Fig. 1b). This process is akin to the jump of a vacancy located on the edge dislocation core along the glide $[111]$ direction, which corresponds to a nearest-neighbor jump in a bcc lattice. The rate of this process can be written as:

$$q_m^{\text{jog}}(T) = \nu'_0 \exp \left(- \frac{\Delta H_m^\perp + \Delta E_{\text{el}}^{\text{jog}}}{kT} \right) \quad (2)$$

where ν'_0 is the jump attempt frequency and ΔH_m^\perp is the vacancy migration enthalpy, which incorporates contributions from the stress state at the super-jog location, and $\Delta E_{\text{el}}^{\text{jog}}$ is the extra elastic energy incurred by the bending of dislocation segments adjacent to the super-jog (as shown in Fig. 1b). Both of these quantities will be defined and calculated in Sec. 2.3. The above rate must be defined for both forward and backward jumps, with the direction of the jump assigned by defining the resolved shear stress as positive when it creates a force aligned with the glide direction.

A summary of the properties of each type of event is given in Table 1.

¹The function $\lfloor x \rfloor$ is the mathematical floor function.

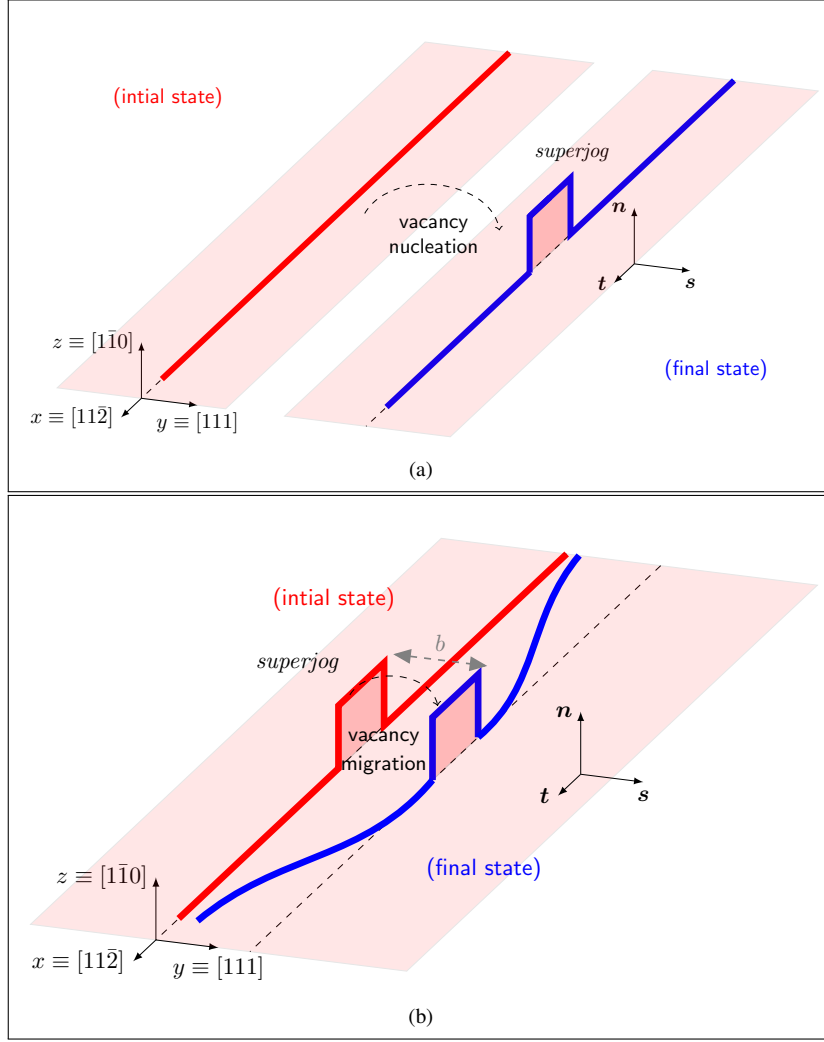


Figure 1: Modes of super-jog evolution. (a) super-jog generation on a straight dislocation line. This mode of motion requires vacancy nucleation. (b) Direct translation along the slip direction s . This mode of motion requires a vacancy jump.

Table 1: Summary of super-jog transitions.

Segment	Rate	Definition	Distance
super-jog (nucleation)	q_n^{jog}	eq. (1)	(super-jog dimensions: $h \times w$)
super-jog (forward/backward)	q_m^{jog}	eq. (2)	b

Using kMC, the set of event rates is sampled at each iteration and the appropriate process is selected and executed. Time is evolved as a Poisson variate:

$$\delta t = -\frac{\log \eta}{R_t} \quad (3)$$

where η is a uniform random number, $R_t = \sum_{\alpha=n,m} \left(\sum_j q_\alpha^{\text{jog}} \right)$, and the subindices α and i apply to the type of transition (' n ' nucleation, ' m ' migration) and to the number of existing super-jogs, respectively. In between thermal events, i.e., during a time δt , the dislocation evolves elastically in response to the existing stresses using a suitable DD model (explained in Sec. 2.2). A flow diagram of the numerical method is given in Appendix A, Figure A.9.

2.2. Dislocation dynamics model

The DD model must be sensitive to the scale of discrete steps on the dislocation line to capture the formation of vacancy induced jogs. As such, the main difference between the dislocation dynamics approach used here and standard DD codes [66] is that the positions of the nodes delimiting the jogs are constrained to have specific lengths. Beyond that, dislocation segments interact in an isotropic elastic manner with one another using the elastic constants of the alloy obtained with the potentials described in Sec. 2.3.

As is customary in most DD formulations, the segment glide velocity v_i^{gl} is linearly dependent on stress as:

$$v_i^{\text{gl}} = \frac{b\Delta\tau}{B_i(T, \theta)} \quad (4)$$

where $b = \|\mathbf{b}\|$ is the Burgers vector's modulus, θ represents the dislocation character ($\cos \theta = \mathbf{s} \cdot \mathbf{t}$, where $\mathbf{s} = b^{-1}\mathbf{b}$ is the slip direction and \mathbf{t} the local line tangent), B_i is a temperature-dependent drag coefficient, and $\Delta\tau$ is the excess glide stress, obtained as the difference between the resolved shear stress τ_{RSS} calculated at the segment or nodal position and a temperature and dislocation character dependent critical stress, τ_c which is a material constant.

$$\Delta\tau = \tau_{\text{RSS}} - \tau_c(T, \theta) \quad (5)$$

with:

$$\tau_c(T, \theta) = \tau_c^{\text{screw}}(T) \cos^2 \theta + \tau_c^{\text{edge}}(T) \sin^2 \theta \quad (6)$$

Likewise, for the drag coefficient B_i , the same dependences on T and θ are used:

$$B_i(T, \theta) = B^{\text{screw}}(T) \cos^2 \theta + B^{\text{edge}}(T) \sin^2 \theta \quad (7)$$

The parameters $\tau_c^{\text{screw}}(T)$, $\tau_c^{\text{edge}}(T)$, $B^{\text{screw}}(T)$, and $B^{\text{edge}}(T)$ are temperature dependent critical stresses and glide friction coefficients for screw and edge coefficients, respectively. Here we employ coefficients derived from recent results by Yin *et al.* [40] for the Nb-Mo-Ta-W equiatomic system, shown in Figure 2. The numerical expressions for the data in the figure used in the present DD simulations are provided in Table 2. Here we use a shear modulus of

Table 2: Numerical expressions use for the temperature dependence of the coefficients plotted in Fig. 2. T is the absolute temperature in K.

Parameter	Expression	Units
$B^{\text{screw}}(T)$	$3.44 \times 10^{-4} \ln(T) - 8.37 \times 10^{-4}$	Pa·s
$B^{\text{edge}}(T)$	2.12×10^{-4}	Pa·s
$\tau_c^{\text{screw}}(T)$	$1418.0 - 0.7T$	MPa
$\tau_c^{\text{edge}}(T)$	$423.6 - 0.1T$	MPa

$\mu = 94$ GPa and a Poisson ratio of $\nu = 0.33$ [59].

The geometry used in the DD simulations follows a Cartesian coordinate system with axes $x \equiv [11\bar{2}]$, $y \equiv [111]$, and $z \equiv [1\bar{1}0]$ representing, respectively, the dislocation line direction, the plane normal, and the glide direction (along the Burgers vector \mathbf{b}). With such an orientation, an external stress tensor with τ_{yz} as the only nonzero component is applied and added to the total segment-segment elastic stresses at each point. While a shear stress τ_{yz} produces a net force on segments aligned with the z direction, i.e., jog segments, we only allow slip on close-packed $\{110\}$ these segments and thus these segments cannot glide conservatively during the simulations. They can, however, move non-conservatively, which as will be shown is dealt with by the kMC module.

2.3. Model parameterization

2.3.1. Atomistic calculations of vacancy formation and migration energies

The two main processes described earlier are characterized by event rates that involve vacancy transitions at or next to edge dislocation cores. The first one, thermal nucleation of super-jogs, is governed by the vacancy formation energy

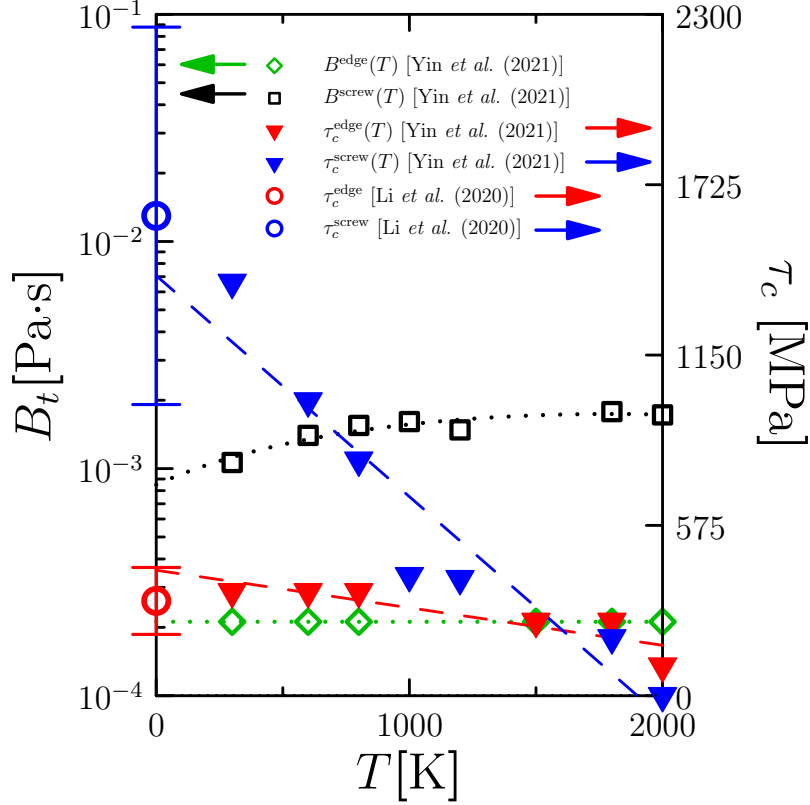


Figure 2: Dislocation critical stresses and friction coefficients from ref. [40]. The two data points for screw and edge at 0 K were obtained using a SNAP potential [59].

at edge dislocation cores, $\Delta E_f^{V@\perp}$. The second one, super-jog translation along the glide direction, is represented by the migration energy along the glide direction of vacancies lying on edge dislocation cores, $\Delta E_m^{0\rightarrow 1}$. For simplicity going forward, we use shorthand notation to refer to $\Delta E_f^{V@\perp}$ and $\Delta E_m^{0\rightarrow 1}$, as E_f^\perp and E_m^\perp , respectively.

To calculate the distribution of E_f^\perp and E_m^\perp , we first construct an edge dislocation dipole in an atomistic supercell using the same procedure described in detail by Hossain and Marian [67]. In this work we use a spectral neighbor analysis potential (SNAP) for the Nb-Mo-Ta-W system, which has been trained against a comprehensive materials database [59, 68]. A value of $a_0 = 3.24 \text{ \AA}$ is obtained for the lattice parameter of the alloy using this potential.

Figure 3a shows the relaxed atomic structure of the dipole visualized according to common neighbor analysis and the dislocation extraction algorithm using Ovito [69], while Fig. 3b shows a side view with the two edge dislocation locations (\perp symbols) and two atomic positions, labeled ‘0’ and ‘1’, at and near the dislocation cores. E_f^\perp is calculated at different ‘0’ locations along the dislocation line. Note that while these locations are crystallographically equivalent, they are ‘chemically’ different, which is the source of the variability in E_f^\perp .

For its part, E_m^\perp is calculated as the migration energy between points ‘0’ and ‘1’, which are separated by an amount equal to the first nearest neighbor distance (equivalent to the Burgers vector’s modulus) with both positions located on the same $[11\bar{2}]$ plane. The corresponding normalized distributions, $p(E_f^\perp)$ and $p(E_m^\perp)$, are provided in Figure 4.

As a point of comparison, the statistical means of $p(E_f^\perp)$ and $p(E_m^\perp)$, denoted by \bar{E}_f^\perp and \bar{E}_m^\perp are tabulated here for the random Nb-Mo-Ta-W system along with the corresponding formation and migration energies in bulk Nb-Mo-Ta-W and in the gray material. As Table 3 shows, formation energies are substantially lower than in the bulk (averages of 0.93 versus 2.40 eV). Critically, however, some of the calculated energies are zero or negative, introducing the possibility for spontaneous vacancy formation. In other words, thermal vacancies are expected to form with considerable ease at edge dislocation cores compared to bulk positions, but, most importantly, in certain locations

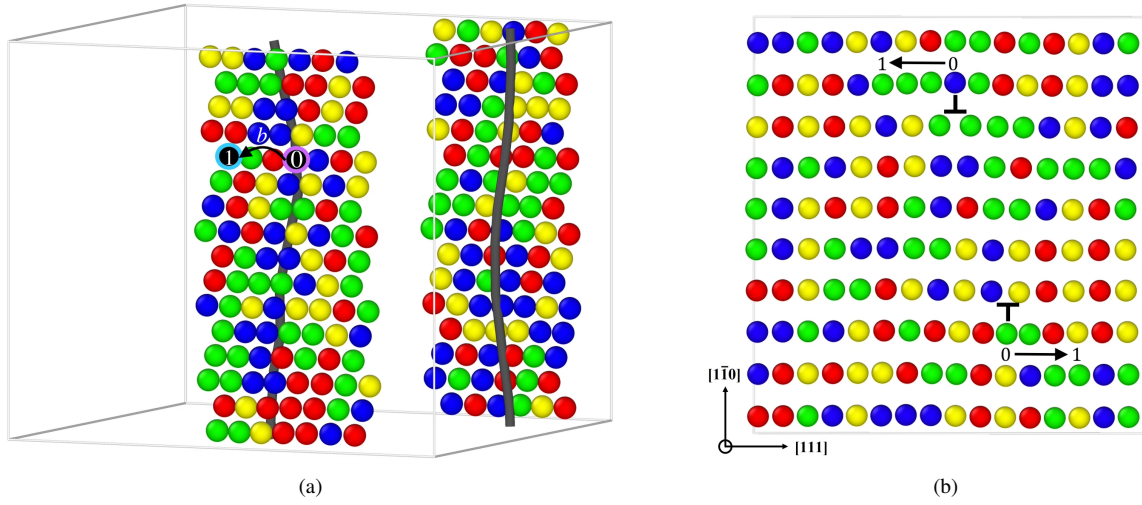


Figure 3: Relaxed edge dislocation dipole utilized for vacancy formation energy calculations. (a) Atomistic representation according to common neighbor analysis and equivalent line representation, both extracted using Ovito [69]. (b) Side view showing the edge pole dislocation locations (\perp symbols) and atoms from three consecutive $[11\bar{2}]$ planes. Atoms are colored by chemical species (green for Nb, red for Mo, blue for Ta, and yellow for W). The atomic positions ‘0’ and ‘1’ (of significance in the text) are indicated in both images. The distance between positions 0 and 1 is equal to the first nearest neighbor distance (i.e., one Burgers vector) with both positions located on the same $[11\bar{2}]$ plane.

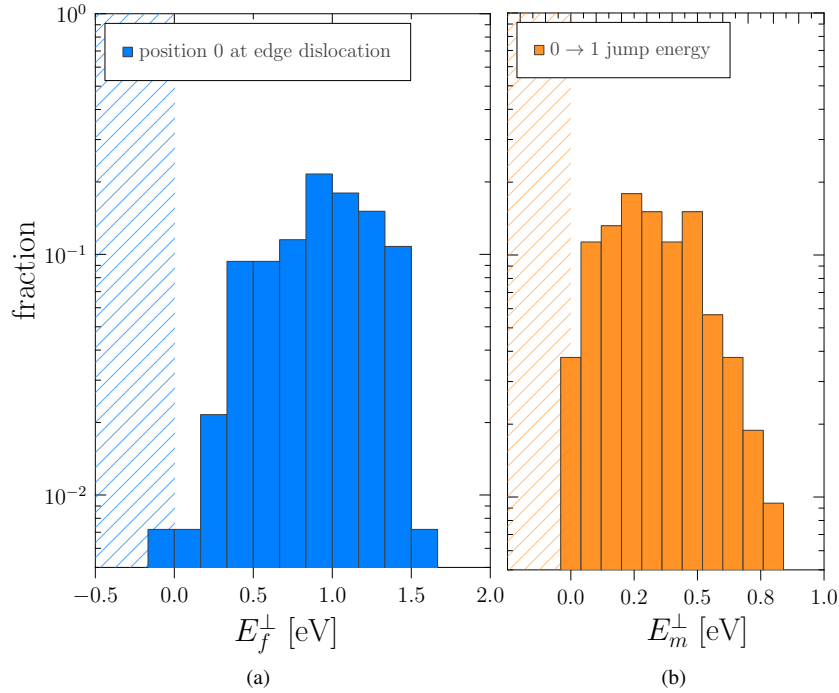


Figure 4: (a) Vacancy formation energy distribution in the Nb-Mo-Ta-W alloy at position ‘0’ near the edge dislocation core in Fig. 3b. (b) Migration energy distribution for the $1 \rightarrow 0$ jump at the edge dislocation core positions shown in Fig. 4a. Negative energies (shaded area in the graphs) signal the spontaneous formation of vacancies and transitions, respectively.

vacancies will form athermally to lower the total local configurational energy around the dislocation. This essentially implies that super-jogs, which are the manifestation of monovacancies in terms of dislocation lines, may naturally

Table 3: Mean energies for the vacancy formation and migration energy distributions at dislocations cores (' \perp ', highlighted in red) and in the bulk ('V'), for both the random Nb-Mo-Ta-W system and the *gray* alloy. The relevant energies are highlighted in red.

Energies [eV]	Nb-Mo-Ta-W	'gray' alloy
\bar{E}_f^\perp	0.93	–
\bar{E}_f^V	2.40	2.62
\bar{E}_m^\perp	0.32	–
\bar{E}_m^V	1.71	1.53

exist along the edge dislocation in equilibrium conditions at any temperature.

2.3.2. Activation enthalpies and attempt rates

Next we turn our attention to the parameters in eqs. (1) and (2). The key quantity to define in eq. (1) is the thermal concentration of super-jogs, $n_0(T)$. In general, $n_0(T) = n_0^* \exp(-E_f^\perp/kT)$, where n_0^* is a pre-factor determined by the crystal geometry. In our case, n_0^* is set by the inverse of the periodicity along the the dislocation line direction, which is equal to $1/w$.

Similarly, the jump rate in eq. (2) can be expressed as:

$$q_m^{\text{jog}}(T) = 2\nu_0' \exp\left(-\frac{\Delta E_m^\perp + \Delta E_{\text{el}}^{\text{jog}}}{kT}\right) \sinh\left(\frac{\Delta\tau (wb^2)}{kT}\right) \quad (8)$$

This expression captures forward and backward jumps² through the sinh term, whose argument is the work done by the excess stress (refer to eq. (5)) to move the super-jog a distance b . The area swept during the process is equal to the width of the super-jog times b , i.e., wb . The product wb^2 comes out to approximately $1.2\Omega_a$ ($\Omega_a = a_0^3/2$). $\Delta E_{\text{el}}^{\text{jog}}$ is the extra elastic energy due to the bending of the dislocation segments adjacent to the super-jog, which is obtained directly by the DD module of the code.

With respect to the attempt frequencies ν_0 and ν_0' , here we adopt a value of 10^{12} Hz for both.

3. Results

3.1. Thermal super-jog concentration

Figure 5 shows an Arrhenius plot of the thermal concentration of super-jogs, n_0 , as a function of temperature in edge dislocations. The figure includes the lower-bound n_0 , characterized by the mean energy of the formation energy distribution in Fig. 4a, given in Table 3 as $\bar{E}_f^\perp = 0.93$ eV, and also the simulated n_0 , obtained by sampling from the distribution in Fig. 4a according to eq. (1) (obtained from 10 independent samplings at each temperature). As the data show, the *effective* formation energies are much lower than 0.93 eV, ranging from 0.02 eV below 400 K to 0.15 eV above 1000 K. Both distributions converge to the common prefactor of $n_0^* = 1/w$ at very high temperatures. Overall the simulated thermal concentration of super-jogs is orders of magnitude larger than that given by the Arrhenius form of n_0 . Moreover, it displays an almost athermal dependence with T , particularly at low temperatures. This is yet another manifestation of the unique properties of compositionally-complex alloys such as Nb-Mo-Ta-W, which display enhanced thermal defect concentrations due to asymmetric samplings of $p(E_f^\perp)$.

²Forward jumps are taken as those for which the stress tensor projected along the Burgers vector's direction results in a positive resolved shear stress along the glide direction, i.e., when $(\sigma : \mathbf{b}) \cdot \mathbf{s} > 0$.

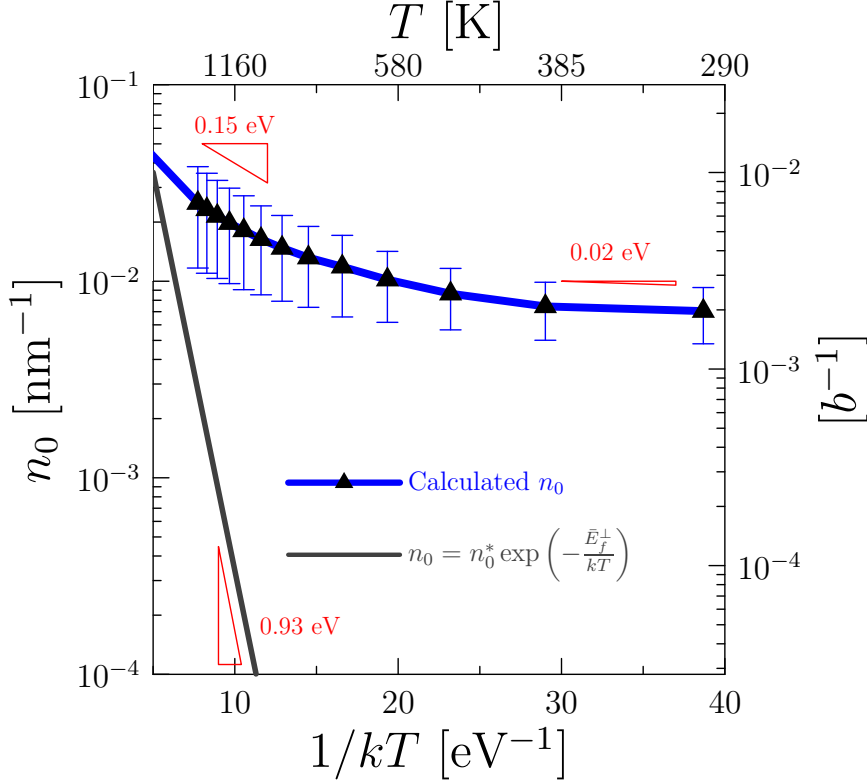


Figure 5: Arrhenius plot of the thermal concentration of super-jogs, n_0 , as a function of temperature on edge dislocations. The figure includes both the lower-bound n_0 , characterized by the mean energy of the formation energy distribution in Fig. 4a, $\bar{E}_f^\perp = 0.93$ eV, and also the simulated n_0 , obtained by sampling from the distribution in Fig. 4a according to eq. (1) (obtained from 10 independent samplings at each temperature).

3.2. Dislocation dynamics under stress

Next we track dislocation motion under stress. We simulate a Frank-Read source with a fixed length L pinned at its endpoints. L is generally obtained as $L \approx (\rho_d)^{-1/2}$, so that its value is consistent with the dislocation density in the material, ρ_d . Values as low as $\rho_d = 5 \times 10^{12} \text{ m}^{-2}$ have been reported in Nb-Mo-Ta-W [70]. However, this is three to four orders of magnitude smaller than dislocation densities measured in other bcc RMEA, such as $2 \times 10^{15} \text{ m}^{-2}$ in Ti-Nb-Hf-Ta [71], $2.1 \times 10^{16} \text{ m}^{-2}$ in Hf-Nb-Ti-Zr [72], or 10^{15} m^{-2} in V-Nb-Mo-Ta-W [63]. Thus, we believe that the value of ρ_d obtained by Zou *et al.* for Nb-Mo-Ta-W [70] may be unrealistically low and, as such, we consider values of $1 \sim 2 \times 10^{15} \text{ m}^{-2}$ as being more representative of the dislocation density in the alloy. This gives rise to average dislocation source lengths on the order of $100 \sim 300b$. Note that, in accordance with the results in Fig. 5, these lengths are sufficient to contain at least one super-jog at temperatures above 580 K. The effect of ρ_d on the model results is further discussed in Sec. 4.3.

3.3. Time evolution of the plastic strain

The plastic strain, ε_p , is the response function in the DD simulations, and is calculated from the aggregate area swept by each dislocation segment during a time iteration [73, 74]. As such, in the DD/kMC simulations we track ε_p as a function of time at different temperatures and stresses. A representative example is shown in Figure 6, where we plot the plastic strain versus time at different temperatures for a dislocation source with length $L = 150b$ containing two super-jogs under 1500 MPa of applied stress. While the ε_p - t curve for $\tau = 500$ K is smooth, indicating the absence of super-jog jumps, the rest of the curves display some roughness associated with sharp super-jog transitions of magnitude $\pm b$. Note that these transitions are both stress and temperature-assisted, as determined by eq. (8).

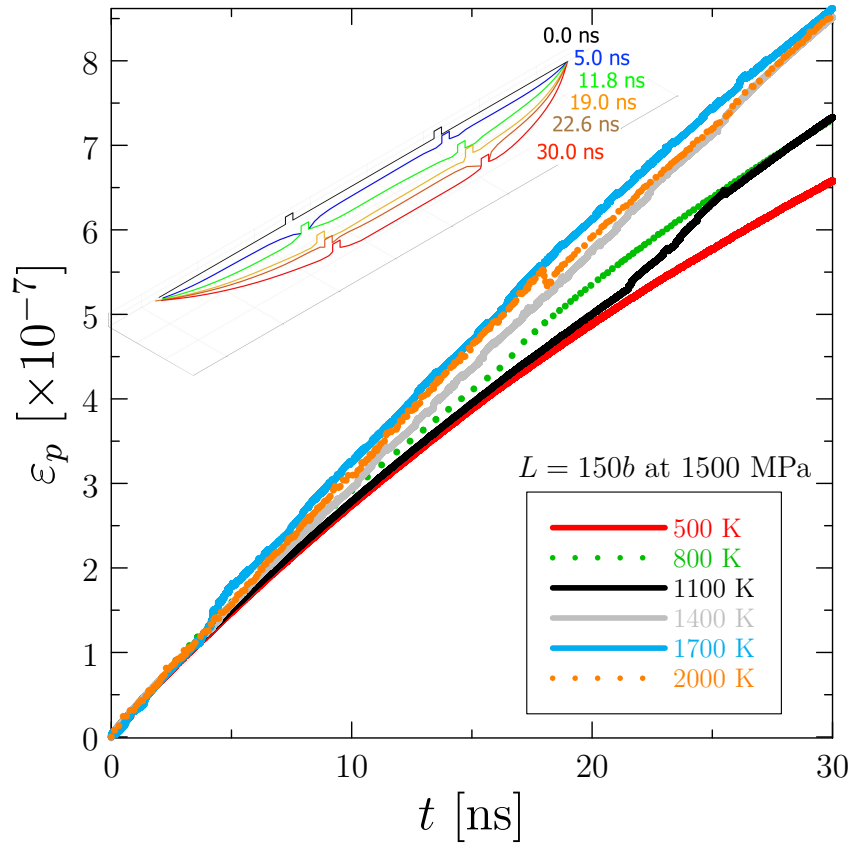


Figure 6: Plastic strain rate as a function of time at several temperatures under an applied stress of 1500 MPa for a dislocation source with a total length of $150b$ containing two super-jogs evenly spread at $+L/3$ and $+2L/3$. The inset shows an overlapping sequence of time frames of the dislocation configuration at 1700 K covering 30 ns of DD/kMC simulation.

The graph shows that, for a fixed dislocation length and super-jog separation, higher temperatures lead to a faster dislocation evolution. This can all be attributed to the diffusional part of the dislocation dynamics, as the viscous contribution, governed by B^{edge} , displays practically no thermal dependence.

3.4. Strain rate-temperature relations

First it is useful to note that the cases without super-jogs are trivially modeled by the Orowan equation for the ideal case of infinite dislocation lengths:

$$\dot{\epsilon}_p = \rho_d b v = \frac{\rho_d b^2}{B^{\text{edge}}} \left(\tau - \Delta\tau - \tau_c^{\text{edge}} \right) = \frac{\rho_d b^2}{B^{\text{edge}}} \left(\tau - \frac{\alpha\mu b}{L} - \tau_c^{\text{edge}} \right) \quad (9)$$

where, from Fig. 2, the only temperature dependence comes via the critical stress τ_c (B^{edge} is a constant, cf. Table 1). As such, the (plastic) strain rate given by eq. (9) is linear both in τ and T with a proportionality constant independent of temperature. From the values in Tables 1 and B.4 and $1/L = \sqrt{\rho_d}$:

$$\dot{\epsilon}_p = 3.72 \times 10^5 (\tau - 850 + 0.1T) \text{ [s}^{-1}\text{]} \quad (10)$$

Next we analyze all the ϵ_p - t curves of dislocation sources in the $75 < L < 310b$ range to extract the relationship between the plastic strain rate, $\dot{\epsilon}_p$, with temperature and stress. The results are shown in Figure 7. Figure 7a gives the stress dependence of $\dot{\epsilon}_p$ for a fixed line length of $150b$ containing two super-jogs. Figure 7b shows its dependence with line length (all containing two super-jogs) for a fixed applied stress of 1000 MPa. Finally, Figure 7c gives the ϵ_p - t relation as a function of the number of super-jogs on a $210b$ line at 1000 MPa. All three figures show cases of

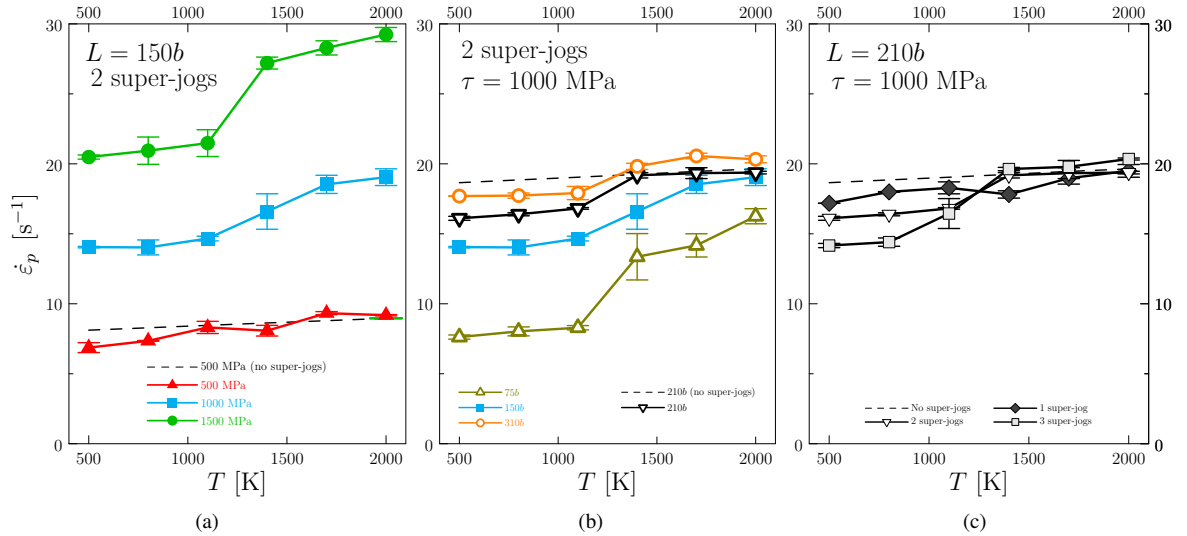


Figure 7: Plastic strain as a function of: (a) stress for a fixed line length of $L = 150b$ and fixed number of super-jogs (two), (b) line length for a fixed applied stress of 1000 MPa and fixed number of super-jogs (two), and (c) number of super-jogs for fixed stress (1000 MPa) and line length ($210b$). The error bars represent the numerical variability obtained from five independent simulations for each case.

straight dislocations containing no-super-jogs for comparison. As expected, the super-jogs confer an extra strength to the dislocation, clearly seen at lower temperatures. This extra strength is negated at above 1100~1300 K, when super-jog diffusion becomes prolific at high temperatures. Thus, in general, the DD/kMC simulations validate the notion that as the temperature increases the super-jogs lose their strengthening power thanks to stress-assisted diffusion. However, that must be coupled to the fact that, as the temperature increases, dislocation lines contain more thermal super-jogs (see Fig. 5), which results in higher strength (i.e., lower plastic strain rates).

4. Discussion

4.1. Physical model

The framework that we use in this paper to study edge dislocation dynamics in RMEA is that of thermally-activated processes modeled using the residence-time algorithm. Thermally-activated events dictate the global timescale of the system, which evolves under elastic forces using the DD method between events. In other words, DD relaxation periods are subordinated to take place within time intervals prescribed by the kMC simulator. This generally fits the timescales on which both methods evolve the dislocation, as typical DD time steps in our calculations are on the order of 10^{-10} s, while sampled time steps from kMC are in the 10^{-3} to 10^{-8} -s range between 500 and 1700 K. The only exception is 2000 K, where the event times are on the order of 10^{-12} s. There, the dislocation evolution is governed by super-jog jumps, without time for elastic relaxation.

We have used a SNAP potential for the Nb-Mo-Ta-W system [59, 68] as the underlying ‘first-principles’ model to calculate defect energetics. This effectively supersedes models that assume that a multielement alloy can be decomposed into a substrate or matrix that possesses the average properties of its elementary constituents and on which every lattice atom constitutes a solute atom [75, 76]. Defect energies do reveal a ‘high entropy’ effect, i.e., they display statistical averages that deviate beyond numerical error from weighted averages of single-valued energies of the individual alloy elements. Specifically, uniform sampling of the energy distributions results in disproportionate numbers of vacancies with energies below the distribution’s mean. What is more, in certain conditions, vacancies appear spontaneously (i.e., athermally) as a consequence of occasional samplings that lead to zero or even negative formation energy values. This effect confers a very particular nature to the Nb-Mo-Ta-W alloy that cannot be surmised from ‘average’ material properties.

What is true for bulk systems is also true for atomistic environments surrounding edge dislocation cores, i.e., vacancies exist thermally (and even spontaneously) on the dislocation line. These vacancies on dislocation lines are topologically equivalent to super-jogs, consistent with a number of works in the literature [55, 77–79]. It is clear that these super-jogs act as pinning points for the dislocation line, increasing the activation stress and strengthening the material [80–83]. The athermal presence of super-jogs can also be put in the context of the relaxed configurations of the lines. The evidence from numerous MD studies in several RMEA consistently points to a ground state of dislocations characterized by rough line shapes [37, 41, 84, 85]. Such states are likely to be micro-states, i.e., reflective of the length scale over which compositional fluctuations take place, which is on the order of one atomic distance. Indeed, such roughness is not captured experimentally with conventional microscopy [86, 87]. From a topological point of view, this roughness may manifest itself as *wiggles* along the dislocation line on the glide plane (i.e., kinks) or as steps on the extra half-plane (jogs). While in our model the effect of the line roughness on the glide plane is subsumed into the temperature dependence of the critical stresses and dislocation friction coefficients, roughness in the form of (super)jogs in the extra half-plane is captured explicitly. This is reminiscent of the existence of cross-kinks in screw dislocation lines in thermal equilibrium recently seen in medium-entropy bcc alloys [56].

Super-jog segments display two potential modes of motion. One is along the line, requiring *climb* by emission or absorption of vacancies. However, our atomistic calculations show that there is no energy benefit in having a super-jog expand laterally by vacancy emission compared to having two super-jogs in adjacent positions on the line. As such, this mode of motion is no different than allowing for natural (thermal) nucleation of super-jogs along the dislocation line. The second degree of freedom is the one considered in our model, i.e., forward/backward translation of a super-jog by a diffusive process. Such process is strongly influenced by the resolved shear stress, favoring motion in the direction along which it is applied. The migration energies for this mode of motion are conceptually equivalent to vacancy migration energies from a position on the dislocation line to the next lattice site along the glide direction, i.e., one Burgers vector distance, which is of course the atomic jump distance in the bcc lattice. As we will show in the next section, this motion leads to a softening of the increased activation stresses due to super-jog pinning.

4.2. An analytical model of edge dislocation strength based on the present numerical results

Using the various contributions to the dislocation evolution model presented in Sec. 2.1, a compact expression for the strength of the material due to edge dislocations can be derived (full derivation provided in Appendix B):

$$\tau = \tau_c^{\text{edge}}(T) + \Delta\tau^*(T) + B^{\text{edge}}(T) \left[\frac{\dot{\epsilon}_0}{\rho_d b^2} - 2q_m^{\text{jog}}(T) \right] \quad (11)$$

where τ_c^{edge} is the critical stress, Table 2, $\Delta\tau^*$ represents the super-jog hardening, eq. (B.3), the term $(B^{\text{edge}}\dot{\epsilon}_0/\rho_d b^2)$ represents the driving force, eq. (B.8), and the term $(2B^{\text{edge}}q_m^{\text{jog}})$, eq. (8), represents stress relief due to super-jog motion. The variation of τ with temperature using the parameters given in Table B.4 is shown in Figure 8, along with each separate contributions from the terms in eq. (11). The figure clearly shows that the evolution of the strength is

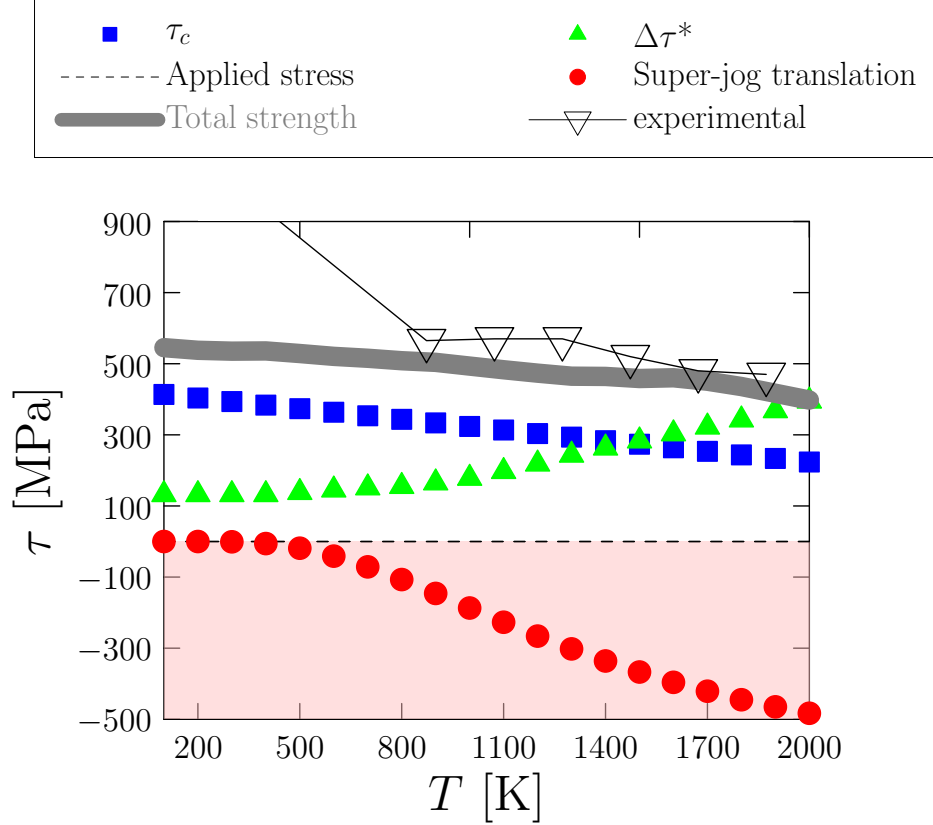


Figure 8: Variation of τ with temperature together with different terms contributing to it in eq. (11) for a strain rate of $\dot{\epsilon} = 10^{-4} \text{ s}^{-1}$. Experimental data from refs. [9, 21].

controlled by the interplay between the intrinsic hardening due to super-jog nucleation and softening due to super-jog diffusion. This interplay results in a monotonic decrease of τ with T as shown in the figure. Note that the effect of the applied stress is negligible compared to super-jog-related mechanisms, amounting to no more than 1 MPa at a strain rate of 10^3 s^{-1} . Most importantly, the strength decreases slowly with temperature, bolstered by a higher thermal concentration of super-jogs (leading to more pinning points) as T increases, and modulated by an easier diffusive glide of the super-jogs with temperature. Such behavior bears a significant resemblance with the temperature dependence of the yield strength of a number of different RMEA [21, 64, 88–90]. As such, we believe that these mechanisms explain –to a large degree– the high temperature strength of these alloys, as quantitatively confirmed by our model and calculations. The obtained response is reminiscent of the high temperature behavior of Ni-based superalloys, where the strength results from a balance between the formation and dissolution of Kear-Wiltsdorf locks, both of which are temperature-enhanced [91].

It is also interesting to derive an expression for the extra strengthening of a RMEA relative to a pure bcc metal under the same loading conditions (cf. Appendix B):

$$\Delta\tau_{\text{RMEA}}(T) \approx \tau_{\text{RMEA}}(T) - \tau_{\text{bcc}}(T) = \tau_c^{\text{edge}}(T) + \Delta\tau^*(T) - 2B^{\text{edge}}(T)q_m^{\text{jog}}(T) \quad (12)$$

This expression gives the terms that contribute to hardening due to the chemical nature of RMEA versus pure or dilute bcc systems. As the equation shows, all terms display a temperature dependence. τ_c^{edge} displays a weak one in the

manner typical of thermal softening, while the other two terms display quasi-exponential (Arrhenius) dependencies. Equation (12) shows that the commonly cited mechanism of lattice fluctuation interactions (local solute interactions) is only one of several terms that contribute to the strength. We believe that non-conservative processes that are unique to RMEA play a fundamental role in explaining the temperature dependence of the alloy strength.

4.3. Discussion on model predictions

Our model results show that the contribution of edge dislocations to the strength of Nb-Mo-Ta-W stems from the balance between two opposing mechanisms. The first is a strengthening contribution associated with a thermal concentration of super-jogs which increases with temperature. The second is a softening effect brought about the thermal motion of the super-jogs, which also increases with temperature. The combination of these two contrary effects dictates the temperature dependence of the edge dislocation contribution.

In terms of comparison with experimental data, we add the yield strength measurements in equiatomic Nb-Mo-Ta-W alloys in Fig. 8 [9, 21]. We see that, while below 800 K there is a gap of over 500 MPa between our model and the experimental measurements, at higher temperatures the match is almost exact. Evidently, the alloy yield strength measured experimentally includes other sources of strengthening beyond edge dislocations, particularly at low temperatures where contribution from screw dislocations, small intermetallic particles and/or short range order could play a role. While this may explain the observed gap, it is clear that edge dislocations should be counted as a significant source of strength in this and other similar RMEA.

We end with a note on the role played by the dislocation density in the strength of edge dislocations. As mentioned in Sec. 3.2, values of ρ_d as low as $5 \times 10^{12} \text{ m}^{-2}$ have been measured for Nb-Mo-Ta-W [70]. However, here we have used more realistic values in the vicinity of 10^{15} m^{-2} to be consistent with most experimental data in bcc RMEA. In eq. (11), the term $(B^{\text{edge}} \dot{\epsilon}_0 / \rho_d b^2)$ represents the driving force and is the only one with an explicit dislocation density dependence. The stress due to this term ranges between 2.7×10^{-9} and 5.4×10^{-7} MPa for $\rho_d = 10^{15}$ and $5 \times 10^{12} \text{ m}^{-2}$, respectively, when $\dot{\epsilon}_0 = 10^{-3} \text{ s}^{-1}$. This effectively renders the driving force term irrelevant in the global picture of strength, which makes the value of the dislocation density in the range of interest also irrelevant.

5. Conclusions

We finish with our main conclusions:

1. We have proposed a new mechanism for edge dislocation dynamics in Nb-Mo-Ta-W alloys. The mechanism provides a qualitative explanation for the elevated intermediate-temperature strength of refractory multi-element alloys, which is governed by non-conservative edge dislocation dynamics.
2. Our mechanism is postulated on the favorable thermal existence –sometimes even spontaneous– of vacancies along edge dislocation lines. These vacancies relax into super-jogs that act as extra pinning points that increase the activation stress. At the same time, these super-jogs are able to diffuse along the glide direction, relieving some of this extra stress. The total strength is a balance between these two processes added on top of the lattice friction due to chemical fluctuations and short-range order.
3. We have developed a numerical model based on a kinetic Monte Carlo module –which captures thermally activated events (super-jog nucleation and translation)– and a discrete dislocation dynamics module –which evolves the line configuration in response to elastic forces– that are coupled to one another via timescale evolution. The global timescale is set by the kMC module on the basis of a Poisson sampling of the thermally activated event rates, while the DD subcycle takes place in between KMC events.
4. All material parameters and alloy energetics have been obtained using a machine-learning SNAP potential. The vacancy formation and migration energies are characterized by distributions with means that deviate from the weighted averages of the elemental constituents of the alloy. Thermal sampling of these distributions results in an equilibrium super-jog concentration that is substantially larger than those predicted by the mean formation energy.
5. An analytical model that captures the essential features of the system yields a strength temperature dependence in excellent qualitative agreement with experimental measurements.

Acknowledgements

This work has been funded by the National Science Foundation under Grant No. DMR-1611342. We thank UCLA's IDRE for computer time allocations on the Hoffman2 supercomputer.

References

References

- [1] B. Cantor, I. Chang, P. Knight, A. Vincent, *Microstructural development in equiatomic multicomponent alloys*, *Materials Science and Engineering: A* 375-377 (2004) 213 – 218. doi:<https://doi.org/10.1016/j.msea.2003.10.257>. URL <http://www.sciencedirect.com/science/article/pii/S0921509303009936>
- [2] J.-W. Yeh, S.-K. Chen, S.-J. Lin, J.-Y. Gan, T.-S. Chin, T.-T. Shun, C.-H. Tsau, S.-Y. Chang, *Nanostructured high-entropy alloys with multiple principal elements: Novel alloy design concepts and outcomes*, *Advanced Engineering Materials* 6 (5) 299–303. arXiv:<https://onlinelibrary.wiley.com/doi/pdf/10.1002/adem.200300567>, doi:10.1002/adem.200300567. URL <https://onlinelibrary.wiley.com/doi/abs/10.1002/adem.200300567>
- [3] L. S. Zhang, G. L. Ma, L. C. Fu, J. Y. Tian, Recent progress in high-entropy alloys, in: *Materials Engineering for Advanced Technologies (ICMEAT 2012)*, Vol. 631 of *Advanced Materials Research*, Trans Tech Publications Ltd, 2013, pp. 227–232. doi:10.4028/www.scientific.net/AMR.631-632.227.
- [4] J. W. Yeh, Y. L. Chen, S. J. Lin, S. K. Chen, High-entropy alloys ? a new era of exploitation, in: *Advanced Structural Materials III*, Vol. 560 of *Materials Science Forum*, Trans Tech Publications Ltd, 2007, pp. 1–9. doi:10.4028/www.scientific.net/MSF.560.1.
- [5] E. J. Pickering, N. G. Jones, *High-entropy alloys: a critical assessment of their founding principles and future prospects*, *International Materials Reviews* 61 (3) (2016) 183–202. arXiv:<https://doi.org/10.1080/09506608.2016.1180020>, doi:10.1080/09506608.2016.1180020. URL <https://doi.org/10.1080/09506608.2016.1180020>
- [6] M. C. G.-W. Y. K. L. Zhang, *High-Entropy Alloys*, Springer, Cham, 2016. doi:<https://doi.org/10.1007/978-3-319-27013-5>.
- [7] D. Miracle, O. Senkov, *A critical review of high entropy alloys and related concepts*, *Acta Materialia* 122 (2017) 448 – 511. doi:<https://doi.org/10.1016/j.actamat.2016.08.081>. URL <http://www.sciencedirect.com/science/article/pii/S1359645416306759>
- [8] M.-H. Tsai, J.-W. Yeh, *High-entropy alloys: A critical review*, *Materials Research Letters* 2 (3) (2014) 107–123. arXiv:<https://doi.org/10.1080/21663831.2014.912690>, doi:10.1080/21663831.2014.912690. URL <https://doi.org/10.1080/21663831.2014.912690>
- [9] O. N. Senkov, D. B. Miracle, K. J. Chaput, J.-P. Couzinie, Development and exploration of refractory high entropy alloys: A review, *Journal of Materials Research* 33 (19) (2018) 3092?3128. doi:10.1557/jmr.2018.153.
- [10] M. C. Gao, J. Qiao, *High-entropy alloys (heas)*, *Metals* 8 (2). doi:10.3390/met8020108. URL <https://www.mdpi.com/2075-4701/8/2/108>
- [11] B. Gludovatz, A. Hohenwarter, D. Catoor, E. H. Chang, E. P. George, R. O. Ritchie, *A fracture-resistant high-entropy alloy for cryogenic applications*, *Science* 345 (6201) (2014) 1153–1158. arXiv:<https://science.sciencemag.org/content/345/6201/1153.full.pdf>, doi:10.1126/science.1254581. URL <https://science.sciencemag.org/content/345/6201/1153>
- [12] S.-q. Xia, W. Zhen, T.-f. Yang, Y. Zhang, Irradiation behavior in high entropy alloys, *Journal of Iron and Steel Research, International* 22 (10) (2015) 879–884.
- [13] S. Xia, M. C. Gao, T. Yang, P. K. Liaw, Y. Zhang, Phase stability and microstructures of high entropy alloys ion irradiated to high doses, *Journal of Nuclear Materials* 480 (2016) 100–108.
- [14] N. K. Kumar, C. Li, K. Leonard, H. Bei, S. Zinkle, Microstructural stability and mechanical behavior of fenimncr high entropy alloy under ion irradiation, *Acta Materialia* 113 (2016) 230–244.
- [15] T. Egami, W. Guo, P. Rack, T. Nagase, Irradiation resistance of multicomponent alloys, *Metallurgical and Materials Transactions A* 45 (1) (2014) 180–183.
- [16] R. Kozak, A. Sologubenko, W. Steurer, *Single-phase high-entropy alloys: an overview*, *Zeitschrift für Kristallographie - Crystalline Materials* 230 (1) (2015) 55 – 68. doi:<https://doi.org/10.1515/zkri-2014-1739>. URL <https://www.degruyter.com/view/journals/zkri/230/1/article-p55.xml>
- [17] *High-Entropy Alloys: Formation and Properties*, Vol. ASME 2018 Symposium on Elevated Temperature Application of Materials for Fossil, Nuclear, and Petrochemical Industries of Pressure Technology, v001T01A004. arXiv:<https://asmedigitalcollection.asme.org/PT/proceedings-pdf/ETAM2018/40764/V001T01A004/2381193/v001t01a004-etam2018-6732.pdf>, doi:10.1115/ETAM2018-6732. URL <https://doi.org/10.1115/ETAM2018-6732>
- [18] O. Senkov, J. Miller, D. Miracle, C. Woodward, Accelerated exploration of multi-principal element alloys for structural applications, *Calphad* 50 (2015) 32–48.
- [19] D. B. Miracle, J. D. Miller, O. N. Senkov, C. Woodward, M. D. Uchic, J. Tiley, *Exploration and development of high entropy alloys for structural applications*, *Entropy* 16 (1) (2014) 494–525. doi:10.3390/e16010494. URL <https://www.mdpi.com/1099-4300/16/1/494>
- [20] Y. Zhang, T. Zuo, Z. Tang, M. Gao, K. Dahmen, P. Liaw, Z. Lu, Microstructures and properties of high-entropy alloys, *Progress in Materials Science* 61 (2014) 1–93. doi:10.1016/j.pmatsci.2013.10.001.

- [21] O. Senkov, G. Wilks, J. Scott, D. Miracle, **Mechanical properties of $\text{Nb}_{25}\text{Mo}_{25}\text{Ta}_{25}\text{W}_{25}$ and $\text{V}_{20}\text{Nb}_{20}\text{Mo}_{20}\text{Ta}_{20}\text{W}_{20}$ refractory high entropy alloys**, *Intermetallics* 19 (5) (2011) 698 – 706. doi:<https://doi.org/10.1016/j.intermet.2011.01.004>. URL <http://www.sciencedirect.com/science/article/pii/S0966979511000185>
- [22] Y. Zou, S. Maiti, W. Steurer, R. Spolenak, **Size-dependent plasticity in an $\text{Nb}_{25}\text{Mo}_{25}\text{Ta}_{25}\text{W}_{25}$ refractory high-entropy alloy**, *Acta Materialia* 65 (2014) 85 – 97. doi:<https://doi.org/10.1016/j.actamat.2013.11.049>. URL <http://www.sciencedirect.com/science/article/pii/S1359645413009075>
- [23] H. Yao, J.-W. Qiao, M. C. Gao, J. A. Hawk, S.-G. Ma, H. Zhou, **Monbtav medium-entropy alloy**, *Entropy* 18 (5). doi:[10.3390/e18050189](https://doi.org/10.3390/e18050189). URL <https://www.mdpi.com/1099-4300/18/5/189>
- [24] F. Körmann, M. H. Sluiter, **Interplay between lattice distortions, vibrations and phase stability in nbmotaw high entropy alloys**, *Entropy* 18 (8). doi:[10.3390/e18080403](https://doi.org/10.3390/e18080403). URL <https://www.mdpi.com/1099-4300/18/8/403>
- [25] H. Yao, J. Qiao, J. Hawk, H. Zhou, M. Chen, M. Gao, **Mechanical properties of refractory high-entropy alloys: Experiments and modeling**, *Journal of Alloys and Compounds* 696 (2017) 1139 – 1150. doi:<https://doi.org/10.1016/j.jallcom.2016.11.188>. URL <http://www.sciencedirect.com/science/article/pii/S09255838816336647>
- [26] H. Döbelstein, M. Thiele, E. L. Gurevich, E. P. George, A. Ostendorf, **Direct metal deposition of refractory high entropy alloy monbtav**, *Physics Procedia* 83 (2016) 624 – 633, laser Assisted Net Shape Engineering 9 International Conference on Photonic Technologies Proceedings of the LANE 2016 September 19-22, 2016 F^rth, Germany. doi:<https://doi.org/10.1016/j.phpro.2016.08.065>. URL <http://www.sciencedirect.com/science/article/pii/S1875389216301729>
- [27] S. A. Kube, S. Sohn, D. Uhl, A. Datye, A. Mehta, J. Schroers, **Phase selection motifs in high entropy alloys revealed through combinatorial methods: Large atomic size difference favors bcc over fcc**, *Acta Materialia* 166 (2019) 677 – 686. doi:<https://doi.org/10.1016/j.actamat.2019.01.023>. URL <http://www.sciencedirect.com/science/article/pii/S1359645419300382>
- [28] S.-Y. Chang, C.-E. Li, Y.-C. Huang, H.-F. Hsu, J.-W. Yeh, S.-J. Lin, **Structural and thermodynamic factors of suppressed interdiffusion kinetics in multi-component high-entropy materials**, *Scientific Reports* 4 (1) (2014) 4162.
- [29] D. Beke, G. Erdaglyi, **On the diffusion in high-entropy alloys**, *Materials Letters* 164. doi:[10.1016/j.matlet.2015.09.028](https://doi.org/10.1016/j.matlet.2015.09.028).
- [30] S. Zhao, Y. Osetsky, Y. Zhang, **Preferential diffusion in concentrated solid solution alloys: Nife, nico and nicocr**, *Acta Materialia* 128 (2017) 391–399. doi:<https://doi.org/10.1016/j.actamat.2017.01.056>. URL <https://www.sciencedirect.com/science/article/pii/S1359645417300812>
- [31] A. Roy, J. Munshi, G. Balasubramanian, **Low energy atomic traps sluggishize the diffusion in compositionally complex refractory alloys**, *Intermetallics* 131 (2021) 107106. doi:<https://doi.org/10.1016/j.intermet.2021.107106>. URL <https://www.sciencedirect.com/science/article/pii/S0966979521000236>
- [32] V. Soni, O. N. Senkov, B. Gwalani, D. B. Miracle, R. Banerjee, **Microstructural design for improving ductility of an initially brittle refractory high entropy alloy**, *Scientific Reports* 8 (1) (2018) 8816. doi:[10.1038/s41598-018-27144-3](https://doi.org/10.1038/s41598-018-27144-3). URL <https://doi.org/10.1038/s41598-018-27144-3>
- [33] J.-W. Yeh, S.-J. Lin, **Breakthrough applications of high-entropy materials**, *Journal of Materials Research* 33 (19) (2018) 3129?3137. doi:[10.1557/jmr.2018.283](https://doi.org/10.1557/jmr.2018.283).
- [34] J.-P. Couzinié, L. Liliensten, Y. Champion, G. Dirras, L. Perrière, I. Guillot, **On the room temperature deformation mechanisms of a tizrhnfbta refractory high-entropy alloy**, *Materials Science and Engineering: A* 645 (2015) 255–263.
- [35] J.-P. Couzinié, G. Dirras, **Body-centered cubic high-entropy alloys: From processing to underlying deformation mechanisms**, *Materials Characterization* 147 (2019) 533–544.
- [36] Y. Bu, Y. Wu, Z. Lei, X. Yuan, H. Wu, X. Feng, J. Liu, J. Ding, Y. Lu, H. Wang, et al., **Local chemical fluctuation mediated ductility in body-centered-cubic high-entropy alloys**, *Materials Today* 46 (2021) 28–34.
- [37] B. Chen, S. Li, H. Zong, X. Ding, J. Sun, E. Ma, **Unusual activated processes controlling dislocation motion in body-centered-cubic high-entropy alloys**, *Proceedings of the National Academy of Sciences* 117 (28) (2020) 16199–16206.
- [38] C. Lee, F. Maresca, R. Feng, Y. Chou, T. Ungar, M. Widom, K. An, J. D. Poplawsky, Y.-C. Chou, P. K. Liaw, et al., **Strength can be controlled by edge dislocations in refractory high-entropy alloys**, *Nature communications* 12 (1) (2021) 1–8.
- [39] C. Lee, G. Kim, Y. Chou, B. L. Musicó, M. C. Gao, K. An, G. Song, Y.-C. Chou, V. Keppens, W. Chen, et al., **Temperature dependence of elastic and plastic deformation behavior of a refractory high-entropy alloy**, *Science Advances* 6 (37) (2020) eaaz4748.
- [40] S. Yin, Y. Zuo, A. Abu-Odeh, H. Zheng, X.-G. Li, J. Ding, S. P. Ong, M. Asta, R. O. Ritchie, **Atomistic simulations of dislocation mobility in refractory high-entropy alloys and the effect of chemical short-range order**, *Nature communications* 12 (1) (2021) 1–14.
- [41] S. Rao, C. Varvenne, C. Woodward, T. Parthasarathy, D. Miracle, O. Senkov, W. Curtin, **Atomistic simulations of dislocations in a model bcc multicomponent concentrated solid solution alloy**, *Acta Materialia* 125 (2017) 311–320.
- [42] E. Ma, **Unusual dislocation behavior in high-entropy alloys**, *Scripta Materialia* 181 (2020) 127–133.
- [43] C. G. Schön, **On short-range order strengthening and its role in high-entropy alloys**, *Scripta Materialia* 196 (2021) 113754.
- [44] Y. Shen, D. E. Spearot, **Mobility of dislocations in fenicrcocu high entropy alloys**, *Modelling and Simulation in Materials Science and Engineering* 29 (8) (2021) 085017.
- [45] Z. Wang, C. Liu, P. Dou, **Thermodynamics of vacancies and clusters in high-entropy alloys**, *Physical Review Materials* 1 (4) (2017) 043601.
- [46] Q. Ding, Y. Zhang, X. Chen, X. Fu, D. Chen, S. Chen, L. Gu, F. Wei, H. Bei, Y. Gao, et al., **Tuning element distribution, structure and properties by composition in high-entropy alloys**, *Nature* 574 (7777) (2019) 223–227.
- [47] S. Zhao, **Role of chemical disorder and local ordering on defect evolution in high-entropy alloys**, *Phys. Rev. Materials* 5 (2021) 103604. doi:[10.1103/PhysRevMaterials.5.103604](https://doi.org/10.1103/PhysRevMaterials.5.103604). URL <https://link.aps.org/doi/10.1103/PhysRevMaterials.5.103604>
- [48] J. Byggmästar, K. Nordlund, F. Djurabekova, **Modeling refractory high-entropy alloys with efficient machine-learned interatomic potentials: Defects and segregation**, *Phys. Rev. B* 104 (2021) 104101. doi:[10.1103/PhysRevB.104.104101](https://doi.org/10.1103/PhysRevB.104.104101). URL <https://link.aps.org/doi/10.1103/PhysRevB.104.104101>

- [49] A. Roy, P. Singh, G. Balasubramanian, D. D. Johnson, Vacancy formation energies and migration barriers in multi-principal element alloys, *Acta Materialia* (2022) 117611.
- [50] M. Kabir, T. T. Lau, D. Rodney, S. Yip, K. J. Van Vliet, Predicting dislocation climb and creep from explicit atomistic details, *Physical review letters* 105 (9) (2010) 095501.
- [51] M. Hossain, J. Marian, [Stress-dependent solute energetics in wre alloys from first-principles calculations](https://doi.org/10.1016/j.actamat.2014.07.028), *Acta Materialia* 80 (2014) 107 – 117. doi:<https://doi.org/10.1016/j.actamat.2014.07.028>. URL <http://www.sciencedirect.com/science/article/pii/S1359645414005461>
- [52] M. Zehetbauer, Effects of non-equilibrium vacancies on strengthening, in: *Key Engineering Materials*, Vol. 97, Trans Tech Publ, 1994, pp. 287–306.
- [53] F. Louchet, B. Viguier, Ordinary dislocations in γ -tial: cusp unzipping, jog dragging and stress anomaly, *Philosophical Magazine A* 80 (4) (2000) 765–779.
- [54] S. Rao, C. Woodward, B. Akdim, O. Senkov, D. Miracle, Theory of solid solution strengthening of bcc chemically complex alloys, *Acta Materialia* 209 (2021) 116758.
- [55] Q. Feng, S. H. Whang, Cross-slip and glide behavior of ordinary dislocations in single crystal γ -ti–56al, *Intermetallics* 7 (9) (1999) 971–979.
- [56] X. Zhou, S. He, J. Marian, Cross-kinks control screw dislocation strength in equiatomic bcc refractory alloys, *Acta Materialia* 211 (2021) 116875.
- [57] X. Zhou, J. Marian, Temperature and stress dependence of screw dislocation mobility in nb-v-ta alloys using kinetic monte carlo simulations, *Frontiers in Materials* (2021) 520.
- [58] Z. Zhou, Y. Zhou, Q. He, Z. Ding, F. Li, Y. Yang, Machine learning guided appraisal and exploration of phase design for high entropy alloys, *npj Computational Materials* 5 (1) (2019) 1–9.
- [59] X.-G. Li, C. Chen, H. Zheng, Y. Zuo, S. P. Ong, Complex strengthening mechanisms in the nbmotaw multi-principal element alloy, *npj Computational Materials* 6 (1) (2020) 1–10.
- [60] J. Rickman, G. Balasubramanian, C. Marvel, H. Chan, M.-T. Burton, Machine learning strategies for high-entropy alloys, *Journal of Applied Physics* 128 (22) (2020) 221101.
- [61] F. Krmann, A. V. Ruban, M. H. Sluiter, [Long-ranged interactions in bcc nbmotaw high-entropy alloys](https://doi.org/10.1080/21663831.2016.1198837), *Materials Research Letters* 5 (1) (2017) 35–40. arXiv:<https://doi.org/10.1080/21663831.2016.1198837>, doi:10.1080/21663831.2016.1198837. URL <https://doi.org/10.1080/21663831.2016.1198837>
- [62] X. Feng, J. Zhang, Y. Wang, Z. Hou, K. Wu, G. Liu, J. Sun, [Size effects on the mechanical properties of nanocrystalline nbmotaw refractory high entropy alloy thin films](https://doi.org/10.1016/j.ijplas.2017.04.013), *International Journal of Plasticity* 95 (2017) 264 – 277. doi:<https://doi.org/10.1016/j.ijplas.2017.04.013>. URL <http://www.sciencedirect.com/science/article/pii/S074964191630345X>
- [63] S. Xin, M. Zhang, T. Yang, Y. Zhao, B. Sun, T. Shen, Ultrahard bulk nanocrystalline vnbmotaw high-entropy alloy, *Journal of Alloys and Compounds* 769 (2018) 597–604.
- [64] H. Zhang, Y. Zhao, J. Cai, S. Ji, J. Geng, X. Sun, D. Li, High-strength nbmotaw refractory high-entropy alloy with low stacking fault energy eutectic phase via laser additive manufacturing, *Materials & Design* 201 (2021) 109462.
- [65] M. Pozuelo, J. Marian, Microscale deformation controlled by compositional fluctuations in equiatomic nb-mo-ta-w alloys, submitted to *Materials Science and Engineering A* (2022).
- [66] V. Bulatov, W. Cai, J. Fier, M. Hiratani, G. Hommes, T. Pierce, M. Tang, M. Rhee, K. Yates, T. Arsenlis, Scalable line dynamics in paradisi, in: *SC'04: Proceedings of the 2004 ACM/IEEE Conference on Supercomputing*, IEEE, 2004, pp. 19–19.
- [67] M. Hossain, J. Marian, Stress-dependent solute energetics in w–re alloys from first-principles calculations, *Acta Materialia* 80 (2014) 107–117.
- [68] X. Li, [A spectral neighbor analysis potential for nb-mo-ta-w](https://arxiv.org/abs/1912.01789), OpenKIMdoi:10.1038/s41524-020-0339-0. URL <https://arxiv.org/abs/1912.01789>
- [69] A. Stukowski, Visualization and analysis of atomistic simulation data with ovito—the open visualization tool, *Modelling and Simulation in Materials Science and Engineering* 18 (1) (2009) 015012.
- [70] Y. Zou, H. Ma, R. Spolenak, Ultrastrong ductile and stable high-entropy alloys at small scales, *Nature communications* 6 (1) (2015) 1–8.
- [71] P. Thirathipviwat, G. Song, J. Bednarcik, U. Kühn, T. Gemming, K. Nielsch, J. Han, Compositional complexity dependence of dislocation density and mechanical properties in high entropy alloy systems, *Progress in Natural Science: Materials International* 30 (4) (2020) 545–551.
- [72] J. Gubicza, A. Heczal, M. Kawasaki, J.-K. Han, Y. Zhao, Y. Xue, S. Huang, J. L. Lábár, Evolution of microstructure and hardness in hf25nb25ti25zr25 high-entropy alloy during high-pressure torsion, *Journal of Alloys and Compounds* 788 (2019) 318–328.
- [73] A. Arsenlis, W. Cai, M. Tang, M. Rhee, T. Ooppelstrup, G. Hommes, T. G. Pierce, V. V. Bulatov, Enabling strain hardening simulations with dislocation dynamics, *Modelling and Simulation in Materials Science and Engineering* 15 (6) (2007) 553.
- [74] O. Jamond, R. Gatti, A. Roos, B. Devincere, Consistent formulation for the discrete-continuous model: Improving complex dislocation dynamics simulations, *International Journal of Plasticity* 80 (2016) 19–37.
- [75] C. Varvenne, A. Luque, W. A. Curtin, [Theory of strengthening in fcc high entropy alloys](https://doi.org/10.1016/j.actamat.2016.07.040), *Acta Materialia* 118 (2016) 13. 164–176. doi:10.1016/j.actamat.2016.07.040. URL <http://infoscience.epfl.ch/record/222039>
- [76] F. Maresca, W. A. Curtin, Mechanistic origin of high strength in refractory bcc high entropy alloys up to 1900k, *Acta Materialia* 182 (2020) 235–249.
- [77] N. Shiotani, H. Kimura, R. Hasiguti, R. Maddin, The mechanism of hardening in quenched aluminum, *Acta Metallurgica* 15 (2) (1967) 287–296.
- [78] S. Kitajima, H. Kurishita, Y. Sakurai, Yielding mechanism of highly perfect copper single crystals, *Memoirs of the Faculty of Engineering, Kyushu University* 69 (3).
- [79] K. Srivastava, S. I. Rao, J. A. El-Awady, Unveiling the role of super-jogs and dislocation induced atomic-shuffling on controlling plasticity in magnesium, *Acta Materialia* 161 (2018) 182–193.

- [80] J. S. Koehler, *The nature of work-hardening*, Phys. Rev. 86 (1952) 52–59. doi:10.1103/PhysRev.86.52. URL <https://link.aps.org/doi/10.1103/PhysRev.86.52>
- [81] H. SAKA, K. NODA, T. IMURA, Direct observation of dislocation multiplication in iron at low temperatures by hvem, Transactions of the Iron and Steel Institute of Japan 13 (5) (1973) 318–324. doi:10.2355/isijinternational1966.13.318.
- [82] E. Martinez, J. Marian, A. Arsenlis, M. Victoria, J. Perlado, A dislocation dynamics study of the strength of stacking fault tetrahedra. part i: interactions with screw dislocations, Philosophical Magazine 88 (6) (2008) 809–840.
- [83] L. Song, J. Lin, J. Li, Ordinary dislocation configurations in high nb-containing tial alloy deformed at high temperatures, Philosophical Magazine 97 (7) (2017) 515–526.
- [84] S. Rao, B. Akdim, E. Antillon, C. Woodward, T. Parthasarathy, O. Senkov, Modeling solution hardening in bcc refractory complex concentrated alloys: Nbtizr, nb1. 5tizr0. 5 and nb0. 5tizr1. 5, Acta Materialia 168 (2019) 222–236.
- [85] F. Maresca, W. A. Curtin, Theory of screw dislocation strengthening in random bcc alloys from dilute to “high-entropy” alloys, Acta Materialia 182 (2020) 144–162.
- [86] L. Lilensten, J.-P. Couzini, L. Perri?re, A. Hocini, C. Keller, G. Dirras, I. Guillot, *Study of a bcc multi-principal element alloy: Tensile and simple shear properties and underlying deformation mechanisms*, Acta Materialia 142 (2018) 131 – 141. doi:<https://doi.org/10.1016/j.actamat.2017.09.062>. URL <http://www.sciencedirect.com/science/article/pii/S1359645417308327>
- [87] F. Wang, G. H. Balbus, S. Xu, Y. Su, J. Shin, P. F. Rottmann, K. E. Knipling, J.-C. Stinville, L. H. Mills, O. N. Senkov, et al., Multiplicity of dislocation pathways in a refractory multiprincipal element alloy, Science 370 (6512) (2020) 95–101.
- [88] C.-C. Juan, M.-H. Tsai, C.-W. Tsai, C.-M. Lin, W.-R. Wang, C.-C. Yang, S.-K. Chen, S.-J. Lin, J.-W. Yeh, Enhanced mechanical properties of hfmotatizr and hfmonbtatizr refractory high-entropy alloys, Intermetallics 62 (2015) 76–83.
- [89] O. N. Senkov, D. B. Miracle, K. J. Chaput, J.-P. Couzinie, Development and exploration of refractory high entropy alloys? a review, Journal of materials research 33 (19) (2018) 3092–3128.
- [90] R. Feng, B. Feng, M. C. Gao, C. Zhang, J. C. Neuefeind, J. D. Poplawsky, Y. Ren, K. An, M. Widom, P. K. Liaw, Superior high-temperature strength in a supersaturated refractory high-entropy alloy, Advanced Materials 33 (48) (2021) 2102401.
- [91] A. Vattré, B. Devincere, A. Roos, Dislocation dynamics simulations of precipitation hardening in ni-based superalloys with high γ ? volume fraction, Intermetallics 17 (12) (2009) 988–994.

Appendix A. Computational flow diagram

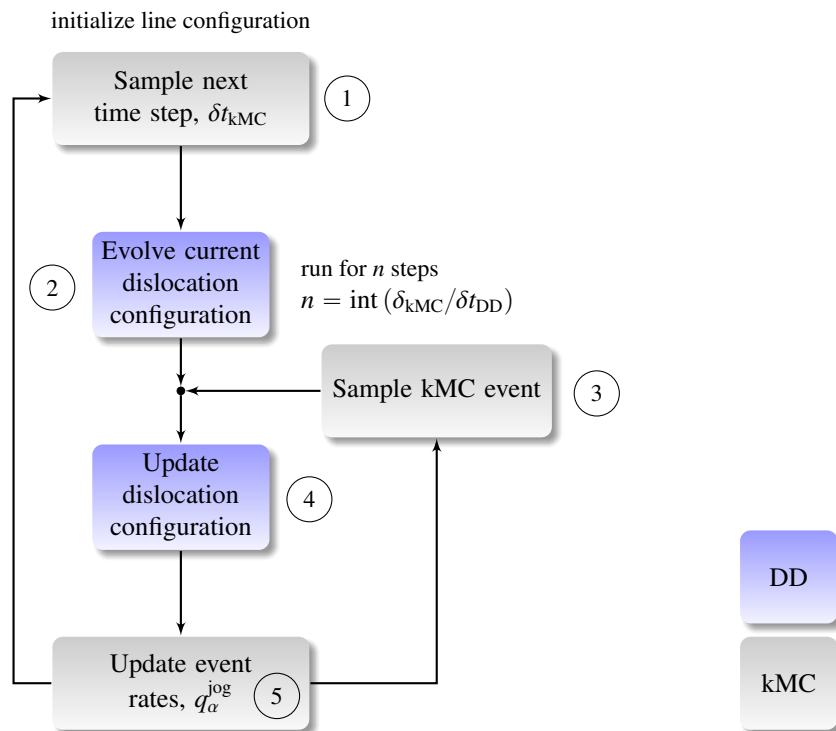


Figure A.9: Flow diagram of the numerical procedure employed here. Processes pertaining to the kMC module are colored in shaded gray, while those pertaining to the DD module are colored in shaded blue. Each box is numbered according to the sequence of steps.

Appendix B. Analytical model of edge dislocation strength due to super-jog evolution

For an edge dislocation source with a length ℓ , one can calculate the activation stress in the standard way as:

$$\Delta\tau = \frac{\alpha\mu b}{\ell}$$

which is independent of temperature if we neglect the thermal softening of the elastic constants of the material. When super-jogs appear, the total dislocation length is shortened into segments of average length ℓ^* :

$$\Delta\tau^*(T) = \frac{\alpha\mu b}{\ell^*(T)} \quad (\text{B.1})$$

where $\ell^*(T)$ is the inverse of the super-jog concentration at temperature T :

$$\ell^*(T) = n_0(T)^{-1} = w \exp\left(\frac{\bar{E}_f^\perp}{kT}\right) \quad (\text{B.2})$$

where we have used $n_0^* = \ell/w$ as the pre-factor of $n_0(T)$, which is equal to the total number of independent nucleation sites along the dislocation line. Equation (B.1) then becomes:

$$\Delta\tau^*(T) = \frac{\alpha\mu b}{w} \exp\left(-\frac{\bar{E}_f^\perp}{kT}\right) \quad (\text{B.3})$$

where we are assuming an exponential temperature dependence of $n_0(T)$ defined by the mean energy value of $p(E_f^\perp)$ (Fig. 4a). Below, this will be replaced with the actual dependence of n_0 on T obtained in Fig. 5. The *excess* stress available for dislocation glide is then obtained by subtracting $\Delta\tau^*(T)$ and $\tau_c^{\text{edge}}(T)$ (Table 2) from the resolved shear stress τ :

$$\Delta\tau_{\text{gl}} = \tau - \left(\Delta\tau^*(T) + \tau_c^{\text{edge}}(T)\right) \quad (\text{B.4})$$

The glide velocity can then be defined as:

$$v_{\text{gl}} = \frac{b\Delta\tau_{\text{gl}}}{B^{\text{edge}}(T)} \quad (\text{B.5})$$

Concurrently, super-jogs can advance along the glide direction with a velocity given by:

$$v_{\text{sj}} = bq_m^{\text{jog}} = 2bv'_0 \exp\left(-\frac{\bar{E}_m^\perp}{kT}\right) \sinh\left(\frac{1.2\Omega_a\tau}{kT}\right) \quad (\text{B.6})$$

where the ‘sinh’ term captures the balance of forward and backward jumps. Here again, we take \bar{E}_m^\perp as representative of the $p(E_m^\perp)$ energy distribution (Fig. 4b). The total velocity of the dislocation line is:

$$v_{\text{tot}} = v_{\text{gl}} + v_{\text{sj}} \quad (\text{B.7})$$

which can be related to a prescribed strain rate $\dot{\epsilon}_0$ using Orowan’s equation:

$$\dot{\epsilon}_0 = b\rho_d v_{\text{tot}} \quad (\text{B.8})$$

where ρ_d is the dislocation density. Combining eqs. (B.5), (B.6), and (B.8), we arrive at:

$$\dot{\epsilon}_0 = b\rho_d \left[\frac{b\Delta\tau_{\text{gl}}}{B^{\text{edge}}(T)} + 2bv'_0 \exp\left(-\frac{\bar{E}_m^\perp}{kT}\right) \right] \quad (\text{B.9})$$

Operating and using the various definitions for the different terms in the above equations, we can write a compact expression for the strength of the material due to edge dislocations:

$$\tau = \tau_c^{\text{edge}}(T) + \Delta\tau^*(T) + B^{\text{edge}}(T) \left[\frac{v_{\text{tot}}}{b} - 2q_m^{\text{jog}}(T) \right] \quad (\text{B.10})$$

with:

$$\begin{aligned}\tau_c^{\text{edge}}(T) &= 423.6 - 0.1T \text{ [MPa]} \\ \Delta\tau^*(T) &= \frac{\alpha\mu b}{w} \exp\left(-\frac{\bar{E}_f^\perp}{kT}\right) \\ v_{\text{tot}} &= \frac{\dot{\epsilon}_0}{\rho_d b} \\ q_m^{\text{jog}}(T) &= v'_0 \exp\left(-\frac{\bar{E}_m^\perp}{kT}\right) \sinh\left(\frac{1.2\Omega_a\tau}{kT}\right)\end{aligned}$$

For convenience, we list all the material constants in Table B.4. Equation (B.10) shows that the sources of strengthen-

Table B.4: Parameters and material constants used to evaluate eq. (B.10).

Parameter	Description	Value	Units	Source
α	hardening coefficient	0.5	–	this work
μ	shear modulus	94	GPa	[59]
a_0	lattice parameter	3.24	Å	this work
b	$a_0\sqrt{3}/2$	2.81	Å	this work
w	$a_0\sqrt{6}/3$	2.64	Å	this work
Ω_a	$a_0^3/2$	1.7×10^{-29}	m ³	this work
B^{edge}	dislocation friction coefficient	2.12×10^{-4}	Pa·s	[40]
\bar{E}_f^\perp	effective super-jog formation energy	0.02~0.13	eV	this work (Fig. 5)
ρ_d	dislocation density	$1 \sim 2 \times 10^{15}$	m ⁻²	Sec. 3.2
v'_0	attempt frequency	10^{13}	Hz	this work
\bar{E}_m^\perp	effective super-jog migration energy	0.32	eV	this work (Fig. 4b)

ing for edge dislocations are the intrinsic lattice stress, τ_c^{edge} (decreases linearly with temperature), the extra stress due to the existence of super-jogs, $\Delta\tau^*(T)$ (increases exponentially with temperature), and the applied stress, $\dot{\epsilon}_0 B^{\text{edge}}/\rho_d b^2$ (independent of temperature). Conversely, the motion of super-jogs, represented by q_m^{jog} , reduces the strength of the material (increasing also exponentially with temperature). However, to obtain the true temperature dependence of the strength of the system, we must substitute the standard Arrhenius expression for $n_0(T)$ in $\Delta\tau^*(T)$, eqs. (B.2) and (B.3), with its actual thermal dependence given in Fig. 5. Such substitution gives rise to the temperature response shown in Fig. 8.

It is also interesting to derive the extra strengthening due to multielement alloy effects. The equivalent of eq. (B.10) for a pure system or dilute alloy would read:

$$\tau_{\text{bcc}} = \tau_c^{\text{edge}}(T) + \alpha\mu b \sqrt{\rho_d} + B^{\text{edge}}(T) \frac{\dot{\epsilon}_0}{b^2 \rho_d} \quad (\text{B.11})$$

i.e., $\Delta\tau(T)^* \equiv \Delta\tau(T)$ takes the standard Taylor form ($\alpha\mu b \sqrt{\rho_d}$) and becomes independent of temperature. Assuming, as it is customary, that $\tau_c^{\text{edge}} \approx 0$ in bcc metals, and that $w \ll \rho_d^{-1/2}$, i.e., neglecting the Taylor hardening term, we can subtract eq. (B.11) from (B.10), we arrive at the extra strengthening associated with RMEA effects:

$$\Delta\tau_{\text{RMEA}}(T) \approx \tau_{\text{RMEA}}(T) - \tau_{\text{bcc}}(T) = \tau_c^{\text{edge}}(T) + \frac{\alpha\mu b}{w} \exp\left(-\frac{\bar{E}_f^\perp}{kT}\right) - 2B^{\text{edge}} v'_0 \exp\left(-\frac{\bar{E}_m^\perp}{kT}\right) \sinh\left(\frac{1.2\Omega_a\tau}{kT}\right) \quad (\text{B.12})$$

This expression gives the terms that contribute to hardening due to the chemical nature of RMEA versus pure or dilute bcc systems. As the equation shows, only the last term has an explicit dependence on stress. In other words, the difference between RMEA and bcc systems decreases with increasing stress on account of the super-jog diffusion term.